Topological defect formation in a quenched ferromagnetic Bose-Einstein condensates

Hiroki Saito,[1] Yuki Kawaguchi,[2] and Masahito Ueda[2,3]

[1]*Department of Applied Physics and Chemistry, The University of Electro-Communications, Tokyo 182-8585, Japan*
[2]*Department of Physics, Tokyo Institute of Technology, Tokyo 152-8551, Japan*
[3]*Macroscopic Quantum Control Project, ERATO, JST, Bunkyo-ku, Tokyo 113-8656, Japan*
(Received 31 October 2006; published 23 January 2007)

We study the dynamics of the quantum phase transition of a ferromagnetic spin-1 Bose-Einstein condensate (BEC) from the polar phase to the broken-axisymmetry phase by changing magnetic field, and find the spontaneous formation of spinor domain walls followed by the creation of polar-core spin vortices. We also find that the spin textures depend very sensitively on the initial noise distribution, and that an anisotropic and colored initial noise is needed to reproduce the Berkeley experiment [Sadler *et al.*, Nature (London) **443**, 312 (2006)]. The dynamics of vortex nucleation and the number of created vortices depend also on the manner in which the magnetic field is changed. We point out an analogy between the formation of spin vortices from domain walls in a spinor BEC and that of vortex-antivortex pairs from dark solitons in a scalar BEC.

I. INTRODUCTION

Topological defects have played a key role in understanding the physics of scalar and spinor superfluids. The first topological defect observed in a gaseous Bose-Einstein condensate (BEC) was a quantized vortex created using the phase imprinting method [1]. Vortices have also been created using a rotating potential [2] and by means of adiabatic spin rotation accompanied by a topological Berry phase [3]. In these methods, topological defect formation is enforced by an external laser or magnetic field. On the other hand, topological defects can also be created spontaneously. The Mermin-Ho texture [4] of superfluid ^{3}He in a cylindrical container involves a coreless vortex. The Kibble-Zurek mechanism [5,6] in a quenched superfluid or in the early universe affords another intriguing example of spontaneous topological defect formation. Thermally nucleated vortices have recently been observed in a gaseous BEC, presenting yet another topological phase transition known as the Berezinskii-Kosterlitz-Thouless transition [7].

Recently, the Berkeley group [8] observed the spontaneous topological defect formation of spin in a spin-1 ^{87}Rb BEC. The atoms were prepared in the $m=0$ state (polar phase in Fig. 1) in a strong magnetic field, where m is the magnetic quantum number. The magnetic field is then lowered below a certain critical value (broken-axisymmetry phase in Fig. 1), where the $m=0$ state becomes dynamically unstable and magnetization grows in a direction perpendicular to the magnetic field, and, consequently, the axisymmetry in the spin space is spontaneously broken [9]. In the experiment, the magnetic field was rapidly decreased across the critical value (as shown by the arrow in Fig. 1)—a process we refer to as "quench"—and the ensuing magnetization dynamics was observed by the spin-sensitive *in situ* measurement [10]. After the quench, it was observed that magnetization grew to form complicated ferromagnetic domains, and that, remarkably, some snapshots of the spatial spin distribution revealed topological spin textures, known as polar-core spin vortices [11].

It has been predicted that a variety of spin textures, such as the staggered domain and helical textures, are created by the quench of the magnetic field [12]. The spontaneous

nucleation of the polar-core vortex has also been predicted in Ref. [13]. The underlying physics in the spontaneous spin-texture formation is spin conservation, which prohibits uniform magnetization.

Motivated by the Berkeley experiment [8], in the present paper we study the dynamics of a spin-1 BEC caused by the quench of the magnetic field from the polar to the broken-axisymmetry phase, and investigate the formation dynamics of the topological spin texture. We show that the spin vortices observed in Ref. [8] are formed in two steps. First, spin domains separated by domain walls develop, breaking the axisymmetry in the spin space. Second, the domains transform into spin vortex-antivortex pairs. We find that the details of the dynamics depend on the initial seed in the $m=\pm 1$ states, which represents residual atoms, quantum fluctuations, and thermal noises, and identify an initial seed that

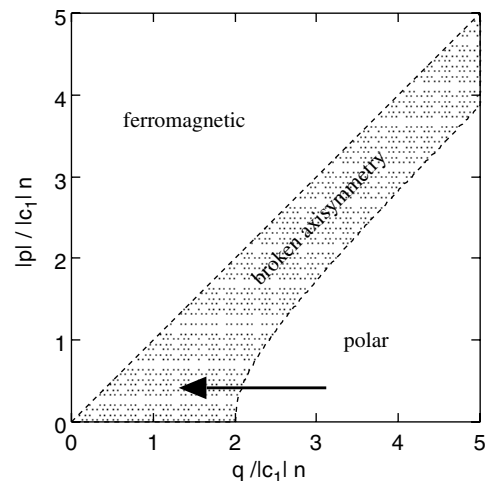FIG. 1. Phase diagram of an homogeneous spin-1 BEC with $c_1 < 0$. In the ferromagnetic phase, the ground state is the $m=1$ state for $p > 0$ and the $m=-1$ state for $p < 0$, while in the polar phase, the ground state is the $m=0$ state. The ground-state wave function in the broken-axisymmetry phase possesses three nonzero components given in Eq. (8), and the spin vector tilts against the applied magnetic field. The arrow indicates the direction of the quench of the magnetic field.

reproduces the experimental results. We also study the quench-time dependence of the number of created spin vortices.

This paper is organized as follows. Section 2 reviews the mean-field theory of the spin-1 BEC and some of its key properties relevant to later discussions. We also point out an analogy between defects in a spinor BEC and those in a scalar BEC in Sec. II C. Section III studies the magnetization dynamics of the trapped system. Sections III C, III D, and III E examine three different kinds of initial noise conditions and identify an appropriate one that captures the main features of the Berkeley experiment. Section III F investigates the dependence of the dynamics on the speed of the quench and on the final value of the quenched magnetic field. Section III G studies the behavior of the growth of the total magnetization, and Sec. IV concludes the paper.

II. MEAN-FIELD THEORY FOR SPIN-1 BEC

A. Formulation of the problem

The zero-temperature mean-field energy of a spinor BEC confined in an optical trapping potential V is given by

$$E = \int d\boldsymbol{r} \left[\sum_m \psi_m^* \left(-\frac{\hbar^2}{2M} \nabla^2 + V \right) \psi_m \right] + E_{\mathrm{int}} + E_B, \quad (1)$$

where M is the mass of the atom and ψ_m is the condensate wave function for atoms in magnetic sublevel m, satisfying $\sum_m \int d\boldsymbol{r} |\psi_m|^2 = N$ with N being the total number of atoms. We define the atomic number density

$$n = \sum_m |\psi_m|^2, \quad (2)$$

and the spin density

$$\boldsymbol{F} = \sum_{mm'} \psi_m^* \boldsymbol{f}_{mm'} \psi_{m'}, \quad (3)$$

where $\boldsymbol{f} = (f_x, f_y, f_z)$ is the vector of the spin-1 matrices. The interaction energy E_{int} for the spin-1 atom has the form [14,15]

$$E_{\mathrm{int}} = \frac{1}{2} \int d\boldsymbol{r}(c_0 n + c_1 \boldsymbol{F}^2), \quad (4)$$

where

$$c_0 = \frac{4\pi\hbar^2}{M} \frac{a_0 + 2a_2}{3}, \quad (5a)$$

$$c_1 = \frac{4\pi\hbar^2}{M} \frac{a_2 - a_0}{3}, \quad (5b)$$

with a_S being the s-wave scattering length for two colliding atoms with total spin S. In the present paper, we consider the case of spin-1 ⁸⁷Rb atoms, and take $a_0 = 101.8a_{\mathrm{B}}$ and $a_2 = 100.4a_{\mathrm{B}}$ [16], where a_{B} is the Bohr radius. The linear and quadratic Zeeman energy E_B under magnetic field $\boldsymbol{B}$ is given by

$$E_B = \int d\boldsymbol{r} \sum_{mm'} \psi_m^* \left[-\frac{1}{2}\mu_{\mathrm{B}}\boldsymbol{B} \cdot \boldsymbol{f} + \frac{\mu_{\mathrm{B}}^2}{4E_{\mathrm{hf}}}(\boldsymbol{B}\cdot\boldsymbol{f})^2 \right]_{mm'} \psi_{m'}, \quad (6)$$

where μ_{B} is the Bohr magneton, E_{hf} is the hyperfine splitting energy, and $1/2$ in the first term is the Landé g factor. The mean-field dynamics of the system is thus described by the multicomponent Gross-Pitaevskii (GP) equation,

$$i\hbar\frac{\partial\psi_{\pm1}}{\partial t} = \left(-\frac{\hbar^2}{2M}\nabla^2 + V \mp \frac{1}{2}\mu_{\mathrm{B}}B + q + c_0 n \right)\psi_{\pm1}$$
$$+ c_1\left(\frac{1}{\sqrt{2}}F_\mp\psi_0 \pm F_z\psi_{\pm1} \right), \quad (7a)$$

$$i\hbar\frac{\partial\psi_0}{\partial t} = \left(-\frac{\hbar^2}{2M}\nabla^2 + V + c_0 n \right)\psi_0 + \frac{c_1}{\sqrt{2}}(F_+\psi_1 + F_-\psi_{-1}), \quad (7b)$$

where $q = (\mu_{\mathrm{B}}B)^2/(4E_{\mathrm{hf}})$, $F_\pm = F_x \pm iF_y$, and the magnetic field is assumed to be in the z direction.

The linear Zeeman terms $\mp\mu_{\mathrm{B}}B/2$ in Eq. (7a) only rotate the spin around the z axis at the Larmor frequency. Going onto the rotating frame of reference by setting $\psi_{\pm1} \rightarrow e^{\mp i\mu_{\mathrm{B}}Bt/(2\hbar)}\psi_{\pm1}$ and $F_\pm \rightarrow e^{\pm i\mu_{\mathrm{B}}Bt/(2\hbar)}F_\pm$, we find that the linear Zeeman terms can be eliminated.

B. Ground state and excitation spectrum

We briefly review the ground state and excitation spectrum for the homogeneous case [9,17]. For spin-1 ⁸⁷Rb atoms, c_1 is negative, and the ground-state phase diagram is given as Fig. 1, where $p = \mu_{\mathrm{B}}B/2 + p_0$ with p_0 being the Lagrange multiplier [17]. Here, p_0 is introduced to set F_z at a prescribed value, since the total magnetization in the z direction is conserved. When the quadratic Zeeman energy q is larger than $2|c_1|n$, the polar phase, $(\psi_1, \psi_0, \psi_{-1}) = \sqrt{n}(0, 1, 0)$, is the ground state. Between the polar and ferromagnetic phases, there is a broken-axisymmetry phase shown as the shaded region in Fig. 1. The order parameter in this phase is given by [9]

$$\psi_{\pm1} = (q \pm p)\sqrt{\frac{p^2 + 2|c_1|nq - q^2}{8|c_1|nq^3}}\sqrt{n}e^{i\chi_{\pm1}}, \quad (8a)$$

$$\psi_0 = \sqrt{\frac{(q^2 - p^2)(p^2 + 2|c_1|nq + q^2)}{4|c_1|nq^3}}\sqrt{n}e^{i(\chi_1 + \chi_{-1})/2}, \quad (8b)$$

where $\chi_{\pm1}$ are arbitrary phases of the $m = \pm1$ states. We note that spin vector $\boldsymbol{F}$ in this phase tilts against the direction of the magnetic field, breaking the axisymmetry spontaneously [9]. The phase boundaries are given by $q = |p|$ and $2|c_1|nq - q^2 + p^2 = 0$, across which the system undergoes the second-order phase transition.

In Sec. III, in an attempt to study the Berkeley experiment we will examine the magnetization dynamics from the initial $m = 0$ state. In order to understand the dynamics qualitatively, we consider the Bogoliubov excitations from the $m = 0$ state

for the homogeneous case. Solving the Bogoliubov–de Gennes equation, we obtain the excitation spectrum as [9,12]

$$E_0 = \sqrt{\varepsilon_k(\varepsilon_k + 2c_0 n)}, \tag{9}$$

$$E_{\pm 1} = \mp \frac{1}{2}\mu_B B + \sqrt{(\varepsilon_k + q)(\varepsilon_k + q + 2c_1 n)}, \tag{10}$$

where $\varepsilon_k = \hbar^2 k^2/(2M)$ with k being the wave number. The mode given in Eq. (9) involves only the $m=0$ state, and can be regarded as a phonon mode, whose excitation energy is always real and positive. The two modes given in Eq. (10) are magnon modes, which transfer the atoms from the $m=0$ state to the $m=\pm 1$ states. The excitation energies $E_{\pm 1}$ are complex for $-q < \varepsilon_k < -2c_1 n - q$. Therefore when c_1 is negative and $q < 2|c_1|n$, the $m=0$ state is dynamically unstable against long-wavelength excitations of the magnon modes. For $q < |c_1|n$, the most unstable wavelength is

$$\lambda_{\mathrm{mu}} = \frac{h}{\sqrt{2M(|c_1|n - q)}}, \tag{11}$$

and the corresponding imaginary part of $E_{\pm 1}$ is $|c_1|n$, giving a characteristic time scale for the dynamical instability as

$$\tau_{\mathrm{mu}} = \frac{\hbar}{|c_1|n}. \tag{12}$$

For a larger magnetic field satisfying $|c_1|n \leq q < 2|c_1|n$, the most unstable wave number is $k=0$, and therefore the system tends to magnetize uniformly. The corresponding time scale is given by $\hbar/[q|q+2c_1 n|]^{1/2}$.

The above Bogoliubov analysis is valid only when the system is homogeneous and deviations from the initial state are small. To investigate regions beyond such restrictions, we will solve full GP equation (7) numerically in Sec. III, and analyze the detailed magnetization dynamics of the trapped system.

C. Topological defects in spinor BECs

Quantized vortices and dark solitons in scalar BECs are topological defects, in which the density vanishes due to the topological constraint on the phase of the wave function. We relate these topological defects in scalar BECs to spin vortices and domain walls in spinor BECs, in which local magnetization vanishes.

We first note that throughout the spin-exchange dynamics the total density $n = |\psi_{-1}|^2 + |\psi_0|^2 + |\psi_1|^2$ remains almost constant because $c_0 \gg |c_1|$. Since the transverse magnetization develops from the $m=0$ state, we also assume that $|\psi_{-1}| = |\psi_1|$ and phases χ_m of ψ_m are related to each other by $\chi_{\pm 1} = \chi_0 \pm \alpha(\mathbf{r}, t)$, where α is an arbitrary function. Substituting these relations in the GP equation (7), we can eliminate ψ_{-1} and ψ_0, obtaining

$$i\hbar \frac{\partial \psi_1}{\partial t} = \left(-\frac{\hbar^2}{2M}\nabla^2 + c_0 n + 2c_1 n - 4c_1 |\psi_1|^2\right)\psi_1, \tag{13}$$

where we drop the trapping potential and the Zeeman terms. If n is assumed to be a constant, Eq. (13) is formally equiva-

lent to the single-component GP equation with a repulsive interaction $c_1 < 0$.

1. Polar-core vortices

The general form of a spin-vortex state is given by

$$\psi_m(\mathbf{r}) = e^{i\gamma_m} e^{ic_m \phi} f_m(r_\perp), \tag{14}$$

where ϕ is the azimuthal angle, γ_m's are global phases, c_m's are integers, and f_m's are real functions of $r_\perp = (x^2 + y^2)^{1/2}$. In Eq. (14), we assume that the system is uniform in the z direction and that the vortex core is located on the z axis. For example, the Mermin-Ho texture has topological charges $c_1 = 0$, $c_0 = 1$, and $c_{-1} = 2$.

The solution to Eq. (13) with a singly quantized vortex is given by

$$\psi_1 = e^{\pm i\phi + i\gamma} f_1(r_\perp),$$

$$\psi_0 = f_0(r_\perp), \tag{15}$$

$$\psi_{-1} = e^{\mp i\phi - i\gamma} f_1(r_\perp),$$

where γ is an arbitrary phase and $f_0^2(r_\perp) + 2f_1^2(r_\perp) = n$. Since the $m=\pm 1$ states have topological defects, $f_1(r_\perp)$ vanishes at $r_\perp = 0$, and the core is then occupied by the $m=0$ (polar) state. The state given by Eq. (15) is therefore referred to as a polar-core vortex state. Equation (13) indicates that f_1 is proportional to $r_\perp/\xi_s$ near $r_\perp = 0$, where

$$\xi_s = \frac{\hbar}{\sqrt{2M|c_1|n}}, \tag{16}$$

and hence the size of the vortex core is characterized by ξ_s.

The spin density for Eq. (15) is given by

$$F_+ = \sqrt{2}(\psi_1^* \psi_0 + \psi_0^* \psi_{-1}) = 2\sqrt{2}e^{\mp i\phi - i\gamma} f_1(r_\perp) f_0(r_\perp), \tag{17}$$

and $F_z = 0$. Equation (17) shows that the spin vector circulates around the z axis with phase winding ∓ 1 and vanishes at $r_\perp = 0$. In fact, the spin current

$$\mathbf{J}_{\mathrm{spin}}^{x,y,z} = \frac{\hbar}{2Mi} \sum_{m,m'} [\psi_m^* F_{mm'}^{x,y,z} \boldsymbol{\nabla} \psi_{m'} - (\boldsymbol{\nabla}\psi_m^*) F_{mm'}^{x,y,z} \psi_{m'}] \tag{18}$$

for Eq. (15) is calculated to be $\mathbf{J}_{\mathrm{spin}}^x = \mathbf{J}_{\mathrm{spin}}^y = 0$ and

$$\mathbf{J}_{\mathrm{spin}}^z = \frac{2\hbar}{Mr_\perp} f_1^2(r_\perp)\mathbf{e}_\phi, \tag{19}$$

where $\mathbf{e}_\phi$ is a unit vector in the azimuthal direction. On the other hand, state (15) has no mass current,

$$\mathbf{J}_{\mathrm{mass}} = \frac{\hbar}{2Mi} \sum_m [\psi_m^* \boldsymbol{\nabla} \psi_m - (\boldsymbol{\nabla}\psi_m^*)\psi_m], \tag{20}$$

and has no orbital angular momentum.

2. Domain walls

Equation (13) has a dark-soliton solution as

$$\psi_1 = e^{-i\mu t/\hbar} \frac{\sqrt{n}}{2} \tanh \frac{z}{\sqrt{2}\xi_s}, \qquad (21)$$

where $\mu = c_0 n - |c_1|n$ and we assume that the planar dark soliton is located at $z=0$. This solution describes a domain wall at $z=0$, since the spin vector $\boldsymbol{F}$ vanishes at $z=0$ and asymptotically approaches a constant vector with opposite directions for $z \to \pm\infty$. The magnitude of transverse magnetization $|F_+|$ is proportional to

$$\tanh \frac{z}{\sqrt{2}\xi_s} \sqrt{1 - \frac{1}{2} \tanh^2 \frac{z}{\sqrt{2}\xi_s}}. \qquad (22)$$

Thus the width of the domain wall is of the same order as the size of the spin vortex.

The planar dark soliton is known to be dynamically unstable against "snake instability" [18,19]. This instability arises for the wavelength longer than the critical wavelength,

$$\lambda_{\mathrm{cr}} = \frac{h}{\sqrt{M|c_1|n}}. \qquad (23)$$

After the distortion by the snake instability, the dark soliton transforms into vortex-antivortex pairs [19]. This phenomenon has been observed in a nonlinear optical medium [20] and in a two-component BEC [21]. In the spinor BEC, an analogous instability causes formation of polar-core vortex-antivortex pairs. We will show in the next section that spin vortices are generated from domain walls by this mechanism.

III. QUENCHING DYNAMICS OF THE TRAPPED SYSTEM

A. Berkeley experiment

In this section, we will numerically simulate the magnetization dynamics in a situation corresponding to the Berkeley experiment [8] and compare the results. We first briefly review the experiment.

The trapping frequencies of the optical potential used in the experiment are given by $(\omega_x, \omega_y, \omega_z) = 2\pi \times (56, 350, 4.3)$ Hz, and the system is effectively quasi-two-dimensional (2D) in the x-z plane. The atoms prepared in the $m=-1$ state are transferred to the $m=0$ state by the field, and the magnetic field of $B=2$ G is applied in the z direction. The number of spin-1 ^{87}Rb atoms in the BEC is 2.1×10^6 with a peak density of $n = 2.8 \times 10^{14}$ cm^{-3}. These conditions give $q/(|c_1|n) \simeq 28.4$, and therefore the prepared state is stable (see Fig. 1). The residual component in each of the $m = \pm 1$ states is less than 0.3%.

The strength of the magnetic field is then suddenly decreased to 50 mG, which corresponds to $q/(|c_1|n) \simeq 0.018$. It follows from Fig. 1 that the $m=0$ state is no longer the ground state and spontaneous magnetization emerges. From $t=50$ to 100 ms, the transverse (x-y direction) magnetization grows exponentially with the time constant of 15 ms. The spin vector varies in space and points in various random directions, and complicated spin textures can be observed. The polar-core vortices are identified in about one-third of the snapshots of the spin distribution, and sometimes several vortices coexist in a single sample. The correlation function for the transverse magnetization,

TABLE I. Length and time scales obtained by the mean-field theory and those observed in the Berkeley experiment [8]. The last row of the right column is blank, since it has not been determined.

Mean-field theory	Experiment
λ_{mu} in Eq. (11) $\simeq 15.1$ μm	wavelength of oscillation in $G_T(\delta r)$ ~ 10 μm (in x) ~ 50 μm (in z)
τ_{mu} in Eq. (12) $\simeq 16$ ms	time constant of $G_T(0)$ $\simeq 15$ ms
ξ_s in Eq. (16) $\simeq 2.4$ μm	size of vortex core $\simeq 3$ μm
λ_{cr} in Eq. (23) $\simeq 21$ μm	length scale of vortex-antivortex pair ?

$$G_T(\delta\boldsymbol{r}) = \mathrm{Re}\left[\frac{\int d\boldsymbol{r} F_-(\boldsymbol{r}) F_+(\boldsymbol{r}+\delta\boldsymbol{r})}{\int d\boldsymbol{r} n(\boldsymbol{r}) n(\boldsymbol{r}+\delta\boldsymbol{r})} \right], \qquad (24)$$

oscillates in both x and z directions. The wavelength of the oscillation in the x direction is ~ 10 μm and that in the z direction is ~ 50 μm. The longitudinal magnetization $G_L(0)$ shows no significant change within $t < 300$ ms, where

$$G_L(\delta\boldsymbol{r}) = \frac{\int d\boldsymbol{r} F_z(\boldsymbol{r}) F_z(\boldsymbol{r}+\delta\boldsymbol{r})}{\int d\boldsymbol{r} n(\boldsymbol{r}) n(\boldsymbol{r}+\delta\boldsymbol{r})}. \qquad (25)$$

The quantities discussed in Sec. II and observed in the experiment are summarized in Table I.

B. Numerical method

We perform full 3D numerical calculations of the GP equation (7) using the Crank-Nicolson scheme with a typical grid size of $\simeq 0.4$ μm. In the numerical calculations, we ignore the linear Zeeman terms in the GP equation for the reason mentioned below Eq. (7). We first prepare the ground state in the $m=0$ state, $\psi_0 = \psi_{\mathrm{ini}}$, by the imaginary-time propagation of the GP equation (7) with $\psi_{\pm 1} = 0$.

If the initial populations of the $m = \pm 1$ states are exactly zero, no spin-exchange dynamics follow within the GP equation. We therefore add small initial seeds to the $m = \pm 1$ states to trigger the spin-exchange dynamics. Possible physical origins of the initial seed include (i) residual atoms due to imperfections in the rf transfer, (ii) quantum fluctuations, and (iii) thermal components. In the experiment, although the residual fraction in each of the $m = \pm 1$ states is suppressed below 0.3% [8], this upper limit corresponds to 6300 atoms, which is still large enough to significantly affect the subsequent dynamics. The spatial distribution of the residual atoms should reflect that of the condensate $\psi_0 = \psi_{\mathrm{ini}}$, while its phase and magnitude can fluctuate spatially due to ex-
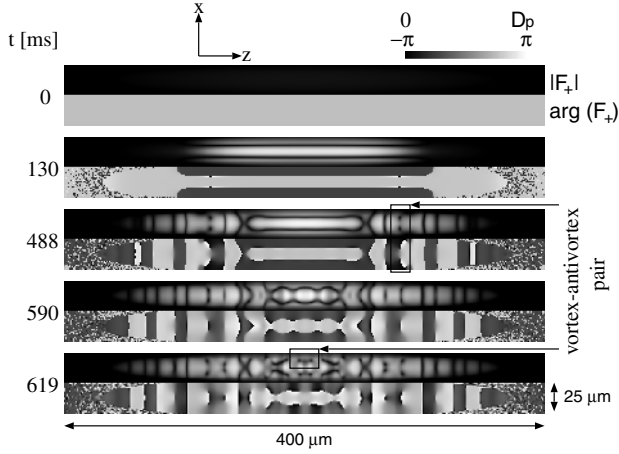
FIG. 2. Magnitude and direction of the spin at $y=0$ for the initial condition in Eq. (26) with $\varepsilon=0.05$. The upper panels show transverse spin density $|F_+|$ and the lower panels show its phase $\arg(F_+)$. The gray scale represents the density from 0 to the initial peak value $D_p=n(\mathbf{r}=\mathbf{0}, t=0)$ for the upper panels, and the phase from $-\pi$ to π for the lower panels. The field of view of each panel is 400 $\times 25$ μm.

perimental noise. Quantum fluctuations trigger the spin-exchange dynamics even if the initial populations in the $m=\pm 1$ states are exactly zero, since the $\hat{\psi}_1^\dagger \hat{\psi}_{-1}^\dagger \hat{\psi}_0^2$ term in the second quantized Hamiltonian transfers the $m=0$ population to the $m=\pm 1$ states. The quantum fluctuations can be taken into account by random noises in the initial state [22]. The thermal component also triggers the growth of the $m=\pm 1$ states having phase fluctuations.

In order to find an appropriate initial seed to reproduce the experimental results and capture the essential mechanism that triggers the magnetization, we will examine three kinds of initial seeds which reflect the shape of the condensate and various types of noise. We will see that the dynamics crucially depend on the nature of the initial seed.

C. Initial seed without noise

In the Berkeley experiment the atoms are first prepared in the $m=-1$ state and then transferred to the $m=0$ state. We suppose that the transfer is imperfect and a small fraction is left in the $m=-1$ state. Thus we assume the initial state to be

$$\psi_1 = 0,$$

$$\psi_0 = \sqrt{1-\varepsilon^2}\,\psi_{\text{ini}}, \qquad (26)$$

$$\psi_{-1} = \varepsilon\,\psi_{\text{ini}},$$

where ε is a small constant. We take $\varepsilon=0.05$ and hence the initial population in the $m=-1$ state is 0.25%, which is consistent with the experimental condition ($<0.3\%$).

Figure 2 shows snapshots of the transverse spin density $|F_+|$ and its direction $\arg(F_+)$. The spin-density profile at $t=130$ ms exhibits three magnetic domains, where the middle one magnetizes in the x direction and the two side ones in the $-x$ direction. The width of each domain $\simeq 8$ μm
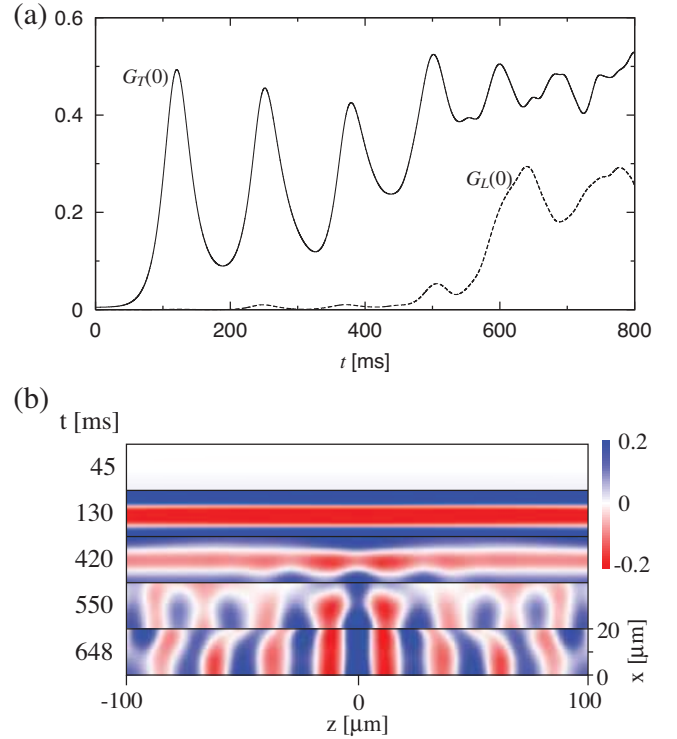

FIG. 3. (Color) (a) Time evolution of $G_T(0)$ (solid curve) and $G_L(0)$ (dashed curve) and (b) $G_T(x,z)$ for the initial condition given in Eq. (26) with $\varepsilon=0.05$.

roughly equals half of the most unstable wavelength (11). As time proceeds, new domains are formed at both ends of the cigar-shaped trap, whose alignment is perpendicular to the central domains (see the snapshot at $t=488$ ms in Fig. 2). Some of them become unstable and spin vortex-antivortex pairs are produced (enclosed by the square at $t=488$ ms in Fig. 2). Afterward, the two central domain walls become wavy ($t=590$ ms), which is followed by the formation of spin vortex-antivortex pairs (enclosed by the square at $t=619$ ms in Fig. 2). Around the spin vortex the direction of the spin vector rotates by 2π in the x-y plane, and the core is occupied by the $m=0$ component. This topological defect is therefore the polar-core vortex discussed in Sec. II C 1. Thus the domain walls are first formed and the polar-core vortices then develop from the domain walls.

We show that the dark-soliton picture discussed in Sec. II C 2 describes the dynamics shown in Fig. 2 very well. The domain walls generated in Fig. 2 can be regarded as dark solitons according to Eqs. (13) and (21). Fitting $|F_+|$ with Eq. (22), we find the width of the domain walls along the z axis at $t=130$ ms is $\simeq 2$ μm, and $\simeq 3.3$ μm for those along the x axis at $t>420$ ms. The snake instability manifests itself as the wavy domain walls at $t=590$ ms with a wavelength $\simeq 19$ μm, which is roughly equal to Eq. (23).

Figure 3(a) shows time evolution of $G_T(0)$ and $G_L(0)$, which indicate the degrees of magnetization in the x-y and z directions, respectively. The transverse magnetization $G_T(0)$ exponentially grows in ~ 100 ms with a time constant $\simeq 16$ ms, which is in good agreement with the experimental observation of 15 ms. The oscillation of $G_T(0)$ at the fre-
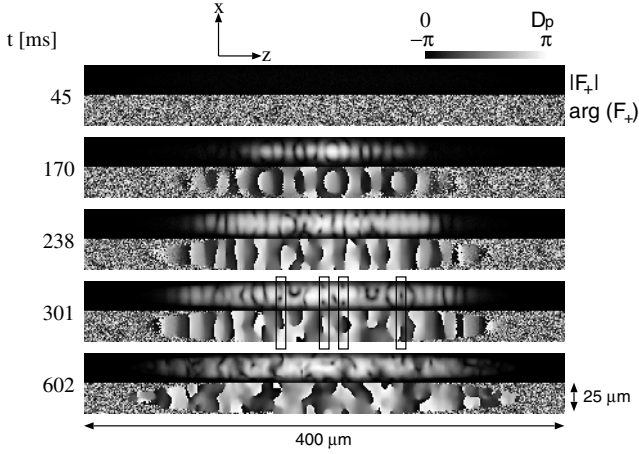
FIG. 4. Magnitude and direction of the spin for the initial condition given in Eq. (27).

quency of ~ 8 Hz is seen from 100 to 600 ms, which was not observed in the experiment. The longitudinal magnetization $G_L(0)$ remains small for $t \lesssim 500$ ms. The transverse correlation function $G_T(\delta r)$ is shown in Fig. 3(b). The stripe pattern in the x direction emerges at $t \simeq 130$ ms, which becomes unstable ($\simeq 420$ ms), transforming into the stripe in the z direction.

The initial growth of the magnetic domains staggered in the x direction is due to the anisotropy in the momentum distribution in the initial seed (26). The Fourier component of the most unstable wavelength (11) contained in the initial seed has the largest weight in the x direction. Since the domain walls staggered in the x direction in Fig. 2(b) were not observed in the experiment, the initial seed in Eq. (26) does not correspond to that in the experiment.

D. Initial seed with white noise

Next we examine the case of white noise as an initial seed in the $m = \pm 1$ states as

$$\psi_1 = \mathcal{N}(f_3 + if_4)f_{env},$$

$$\psi_0 = \mathcal{N}\psi_{ini}, \qquad (27)$$

$$\psi_{-1} = \mathcal{N}(f_1 + if_2)f_{env},$$

where $\mathcal{N}$ is a normalization constant, f_i's are small random numbers obeying the normal distribution $e^{-f^2/(2\sigma^2)}/(\sqrt{2\pi}\sigma)$, and f_{env} is an envelope function. The random number is chosen independently on each grid. We take $\sigma = 2 \times 10^{-4}$, and the initial population in each of the $m = \pm 1$ states is $\simeq 0.23\%$. The envelope function f_{env} is taken to be ψ_{ini}.

Figure 4 shows the distributions of the magnitude and direction of the spin for initial state (27). In contrast to Fig. 2, the domain structure staggered in the z direction first emerges at $t \simeq 170$ ms. The size of the single domain is $\simeq 9$ μm, which is roughly the same as the domain width in Fig. 2 at $t = 130$ ms, reflecting the fact that the domain size is set by the most unstable length scale of the system. Some of
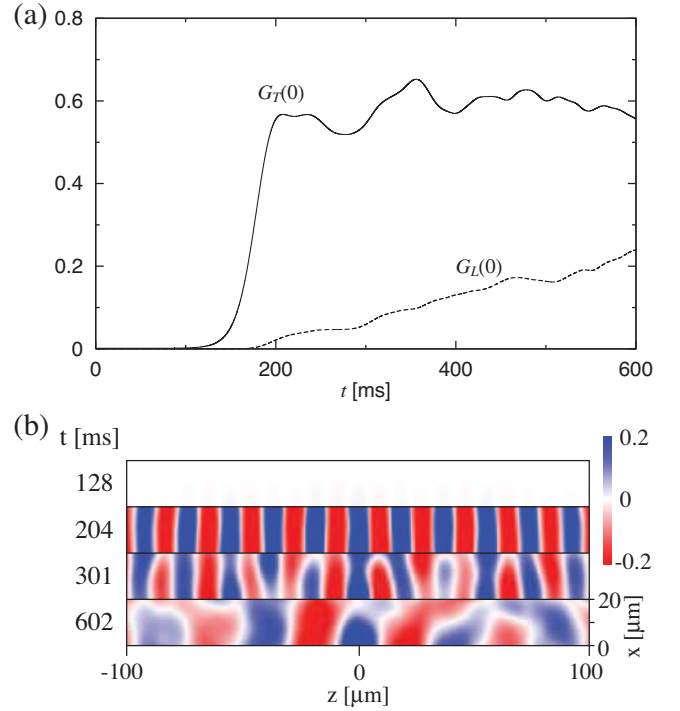

FIG. 5. (Color) (a) Time evolution of $G_T(0)$ (solid curve) and $G_L(0)$ (dashed curve) and (b) $G_T(x,z)$ for the initial condition given in Eq. (27).

the domain walls then develop into the polar-core vortices as shown in the squares in Fig. 4, and the system exhibits complicated spin dynamics similar to the experimental results described in Ref. [8].

Time evolution of the transverse $G_T(0)$ and longitudinal $G_L(0)$ squared magnetization is shown in Fig. 5(a). The time at which $G_T(0)$ rises in Fig. 5(a) is later than that in Fig. 3. This is because the most unstable Fourier component in the initial seed is smaller in the present case due to the broad momentum distribution of the white noise. Figure 5(b) shows the transverse correlation function $G_T(\delta r)$. The clear stripe pattern at $t = 204$ ms indicates the establishment of the long-range correlation over > 200 μm. The stripe pattern is then distorted and its width becomes broader for $t \gtrsim 600$ ms.

We note that the qualitative behaviors in Figs. 4 and 5 are relatively insensitive to the envelope function f_{env} of the initial seed in Eq. (27). We have used $f_{env} = \psi_{ini}$ based on the assumption that the noise reflects the shape of the condensate. However, we find that the results remain qualitatively the same even when the envelope function is not multiplied. We have also confirmed that the results shown above are insensitive to grid size, despite the fact that a random number is initially assigned to each grid and the momentum distribution of the initial noise depends on the grid size.

E. Initial seed with colored noise

The initial states (26) and (27) examined in Secs. III C and III D have been inadequate to reproduce the experimental results. In the experiments, the transverse correlation function $G_T(\delta r)$ oscillates both in the x and z directions and

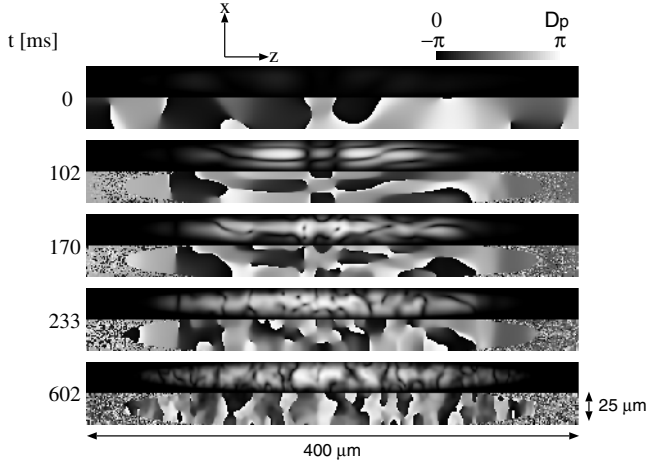FIG. 6. Magnitude and direction of the spin for the initial condition given in Eq. (28) with $\lambda_{\text{cutoff}}=60$ μm.

the wavelength of the oscillation is larger in the z direction than that in the x direction. For the initial seed proportional to ψ_{ini} given in Eq. (26), the domains staggered in the short axis first grow, and for the white noise in Eq. (27), the domains are staggered in the long axis. Therefore we expect that the experimental result can be reproduced using the initial seed that combines Eqs. (26) and (27), i.e., anisotropy and randomness. Since the white noise in Eq. (27) induces the growth of the domains along the x direction (Fig. 4, $t=170$ ms) and the wavelength of the oscillation of $G_T(\delta r)$, $\simeq 18$ μm (Fig. 5, $t=204$ ms), is shorter than that in the experiment, $\simeq 50$ μm, we cut off the short-wavelength components from the white noise. The initial state is thus given by

$$\psi_1 = 0,$$

$$\psi_0 = \mathcal{N}\psi_{\text{ini}}, \tag{28}$$

$$\psi_{-1} = \mathcal{N}f_{\text{cutoff}}f_{\text{env}},$$

where we produce the small noise function f_{cutoff} from the white noise by eliminating the Fourier components whose wavelengths are shorter than λ_{cutoff}. The envelope function f_{env} is taken to be ψ_{ini}.

The results for $\lambda_{\text{cutoff}}=60$ μm are shown in Figs. 6 and 7. The behavior of $G_T(\delta r)$ shown in Fig. 7(b) is similar to that observed in the experiment [8] in that the wavelength of the oscillation in the z direction is larger than that in the x direction. This anisotropy originates from the envelope function $f_{\text{env}}=\psi_{\text{ini}}$ of the initial seed in Eq. (28). The momentum distribution in the x direction of f_{env} is broad and the most unstable wavelength (11) grows in this direction, while in the z direction the typical wavelength in $G_T(\delta r)$ is determined by the cutoff wavelength λ_{cutoff} of the noise.

We note that the qualitative behaviors shown in Fig. 7(b) are independent of the details of the envelope function f_{env} in the initial seed. The similar behaviors can be obtained as long as the size of the envelope function is much larger than the unstable wavelength λ_{mu} in the z direction and is comparable to λ_{mu} in the x direction. In fact, when we use f_{env}
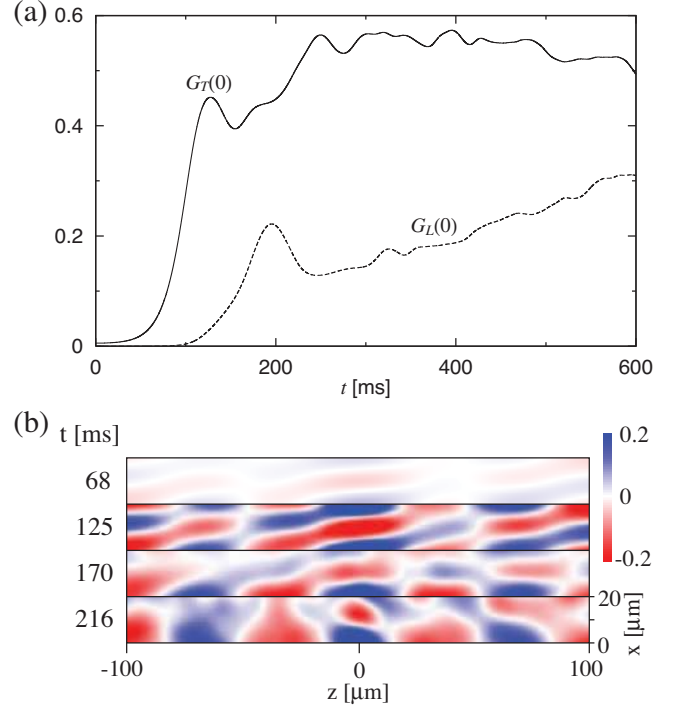

FIG. 7. (Color) (a) Time evolution of $G_T(0)$ (solid curve) and $G_L(0)$ (dashed curve) and (b) $G_T(x,z)$ for the initial condition given in Eq. (28) with $\lambda_{\text{cutoff}}=60$ μm.

$=\psi_{\text{ini}}^2$, qualitatively similar results are obtained.

The behavior of the local transverse magnetization $G_T(0)$ in Fig. 7(a) is also in good agreement with the experimental result. It exponentially increases from $t=50$ to 100 ms with a time constant $\simeq 15$ ms. After $t=100$ ms, $G_T(0)$ gradually increases from 0.4 to 0.6 until $t=300$ ms, which also captures the basic characteristics of the experimental result.

As in Figs. 2 and 4, Fig. 6 shows that the magnetic domains are first formed ($t=102$ ms) followed by the development of some of the domain walls into the polar-core vortices. Thus this process of spin-vortex formation appears rather universal. We also found that the polar-core vortices drift in and out of the condensate in the dynamics.

F. Dependence of the dynamics on quench time and magnetic field

We have so far considered the case of sudden quench, i.e., the magnetic field being suddenly reduced to 50 mG at $t=0$. If the time scale of the quench is longer than ~ 100 ms [time scale in which $G_T(0)$ rises in Fig. 7], the excitations are expected to be suppressed because of the adiabatic theorem.

Figure 8 shows the time evolution for the slow quench, where the initial magnetic field of 530 mG is reduced to 50 mG during 300 ms so that q linearly decreases. We find from Fig. 8(a) that the spin state has nearly a single-domain structure and no spin vortices are created. The transverse $G_T(0)$ and longitudinal $G_L(0)$ components of the squared magnetization are shown in Fig. 8(b). A large value of $G_T(0)\simeq 0.9$ is due to the absence of the spatial spin structure.
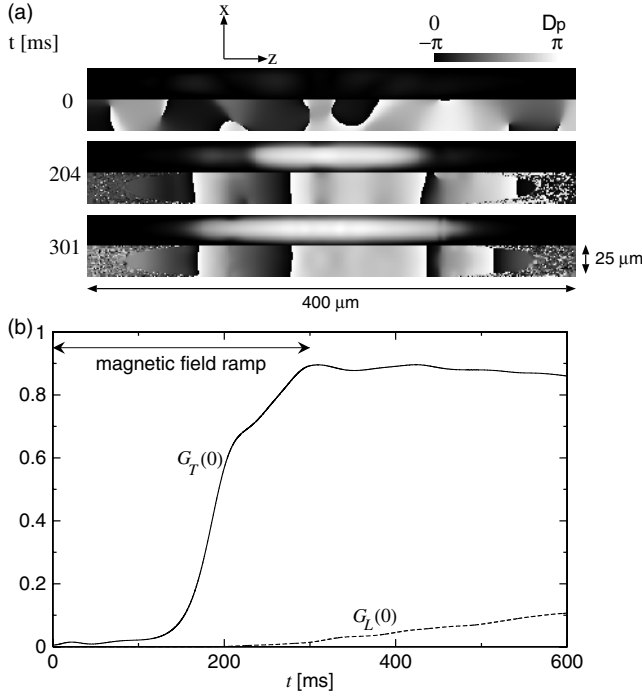
FIG. 8. Time evolution of the system, in which the magnetic field is decreased from 530 to 50 mG during the first 300 ms so that q linearly decreases. The initial condition is the same as in Figs. 6 and 7.

Figure 9 shows the dependence of the number of spin vortices at $t=200$ ms on ramp time. The number of spin vortices decreases with an increase in the ramp time, and the time scale beyond which the spin vortices no longer emerge is given by ~ 100 ms. We note that this time scale coincides with $h/(|c_1|n)$, indicating that the energy scale for the creation of a spin vortex is given by $\sim |c_1|n$. As in the experiment, the number of vortices fluctuates from run to run.
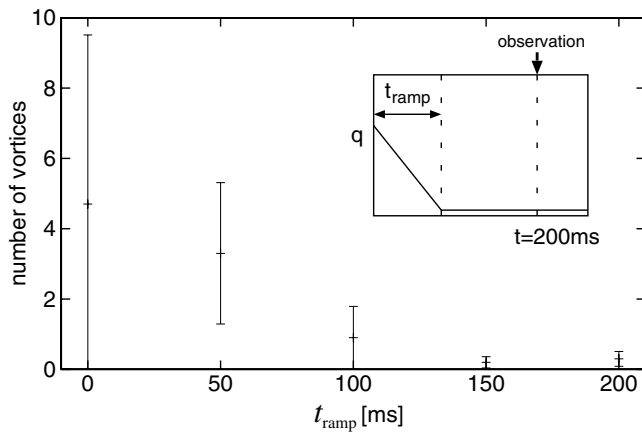

FIG. 9. Ramp time dependence of the number of spin vortices at $t=200$ ms. The initial state is given in Eq. (28) with $\lambda_{cutoff}=60$ μm and the magnetic field is decreased from 530 to 50 mG so that q is linearly ramped down during t_{ramp}. The plots and error bars represent the average and standard deviation with respect to ten runs of simulations for different random numbers to generate the noise.
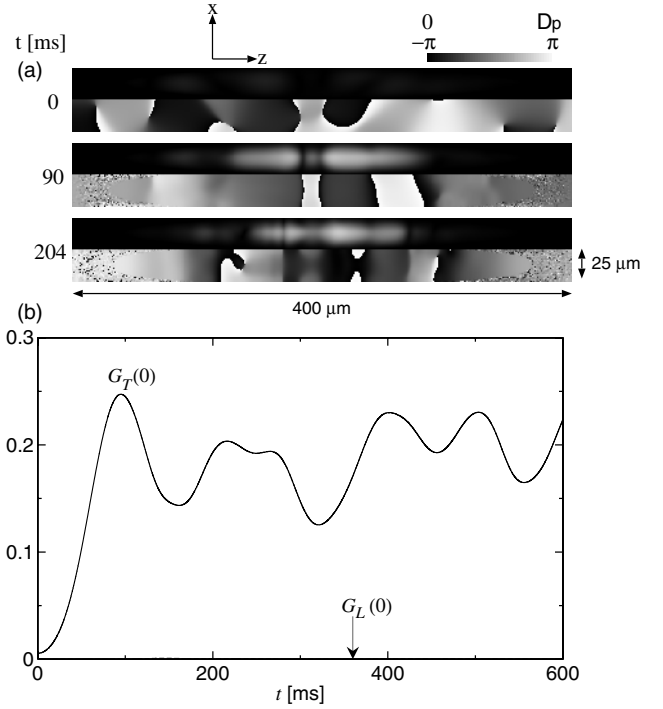

FIG. 10. Time evolution of the system, in which the magnetic field is suddenly decreased to 400 mG at $t=0$. The initial condition is the same as in Figs. 6 and 7.

The result seen in Fig. 9 reminds us of the Kibble-Zurek mechanism [5,6] of the vortex creation in the quenched system, which also depends on the quench time. However, the relationship between the present phenomenon and the Kibble-Zurek mechanism is not straightforward. In the Kibble-Zurek mechanism, each domain is assumed to be created with an independent phase. In the present system, however, the magnetization at each position cannot be independent of that of other positions, since there is the restriction on the change in the total spin, which is clearly seen in the long-range correlation in $G_T(\delta r)$. Gaining a deeper understanding of the relationship between the spin-vortex formation and the Kibble-Zurek mechanism constitutes an interesting and challenging problem which merits further investigation.

The spin-vortex formation is also suppressed if the quench of the magnetic field is made just below the critical strength of the magnetic field, which is given by $q=2|c_1|n$ (see Fig. 1) and corresponds to $B=530$ mG for the peak density. Figure 10 shows the spin dynamics for $B=400$ mG. From Eq. (10), the most unstable wavelength for this magnetic field is $\lambda=\infty$, and the system is more unstable against excitations with larger wavelengths. In Fig. 10(a) therefore only the long-wavelength modes are excited and no spin vortex is formed. In Fig. 10(b), the transverse squared magnetization $G_T(0)$ saturates around 0.2, since $|F_+|$ of the ground state is small near the phase boundary between the broken-axisymmetry and polar phases.

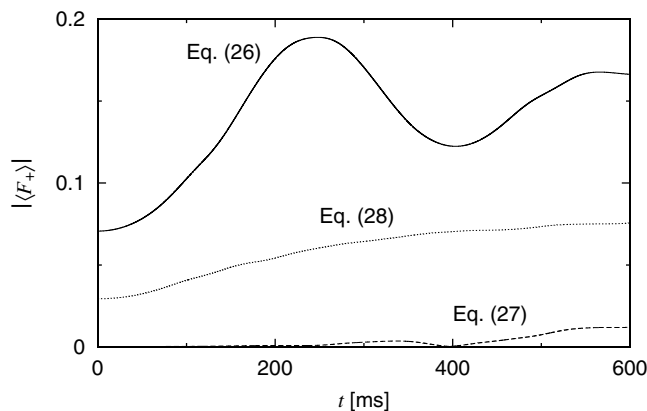### G. Total transverse magnetization

We define the total magnetization as

FIG. 11. Time evolution of the transverse magnetization $|\langle F_+\rangle|$ $= |\int d\mathbf{r} F_+|$ for the dynamics in Fig. 2 (solid curve), Fig. 4 (dashed curve), and Fig. 6 (dotted curve).

$$\langle \mathbf{F} \rangle = \frac{1}{N} \int d\mathbf{r} \mathbf{F}, \qquad (29)$$

where $\mathbf{F}$ is the spin density defined in Eq. (3). If the quadratic Zeeman effect is absent, the z component $\langle F_z \rangle$ and the transverse component $|\langle F_+\rangle|$ are conserved, and the vector $(\langle F_x \rangle, \langle F_y \rangle)$ rotates in the x-y plane at the Larmor frequency determined by the linear Zeeman energy. In the presence of the quadratic Zeeman effect, not only $\langle \mathbf{F} \rangle$ rotates in the x-y plane but also $|\langle F_+\rangle|$ changes with time.

Figure 11 shows time evolution of $|\langle F_+\rangle|$ for the initial conditions given by Eqs. (26)–(28), where the system is quenched by a decrease in the magnetic field to 50 mG at $t=0$ as in Figs. 2–7. For the initial condition (26), $|\langle F_+\rangle|$ has a large initial value $\simeq 0.07$, and reaches a maximum value ~ 0.19. For the initial condition (28), $|\langle F_+\rangle|$ monotonically increases to twice the initial value during 600 ms. Thus the quadratic Zeeman effect generates the transverse component in the total magnetization.

The transverse magnetization $|\langle F_+\rangle|$ may also be changed by the dipole-dipole interaction, since it couples the spin angular momentum with the orbital angular momentum [23,24]. The effect of the dipole-dipole interaction on the transverse magnetization merits further study.

IV. CONCLUSIONS

We have studied the spontaneous magnetization and spin-texture formation of a spin-1 ^{87}Rb BEC, where the initial state is the $m=0$ stationary state ψ_{ini} plus a small seed in the $m = \pm 1$ states.

We have reproduced the polar-core spin-vortex formation observed in the experiment, as shown in Figs. 2, 4, and 6. Typically, the spin vortex is formed in two steps. The magnetic domains are first formed, and then the domain walls transform into the spin vortex-antivortex pairs. This process of vortex formation appears to be universal regardless of various initial conditions.

We have examined three kinds of initial seeds: the one proportional to ψ_{ini}, white noise, and colored noise. The first two seeds produce the domain structures staggered in the short and long axes, respectively (Figs. 2–5). The magnetization developed from the third seed has both characteristics of the first two seeds, and the correlation function oscillates in both the long and the short axes [Fig. 7(a)], in qualitative agreement with the Berkeley experiment [8]. This is due to the fact that the third seed has a broad momentum distribution in the short axis, originating from the shape of ψ_{ini}, and long-wavelength fluctuations in the long axis. From these results, we can conclude that the anisotropy and colored noise in the initial seed are important to account for the experiment. The time evolution of the transverse magnetization $G_T(0)$ is also in close agreement with the experimental result [Fig. 7(b)].

The number of spin vortices created in the magnetization depends on how fast the magnetic field is quenched. When the magnetic field is decreased slowly, the number of nucleated spin vortices decreases (Figs. 8 and 9). We have also shown that the number of spin vortices decreases for the magnetic field close to the critical value (Fig. 10). The transverse component of the total magnetization $|\langle F_+\rangle|$ is changed by the quadratic Zeeman effect, and can exceed twice the initial value (Fig. 11).

We have pointed out a close analogy between the topological defects in the present system and those in a scalar BEC, and that the creation of spin vortex-antivortex pairs from the domain walls is related to the instability in the planar dark solitons. It is of interest to investigate if the counterparts of vortex lattices, multiply quantized vortices, and gray solitons are generated in a ferromagnetic spinor BEC.

[1] M. R. Matthews, B. P. Anderson, P. C. Haljan, D. S. Hall, C. E. Wieman, and E. A. Cornell, Phys. Rev. Lett. **83**, 2498 (1999).

[2] K. W. Madison, F. Chevy, W. Wohlleben, and J. Dalibard, Phys. Rev. Lett. **84**, 806 (2000).

[3] A. E. Leanhardt, A. Görlitz, A. P. Chikkatur, D. Kielpinski, Y. Shin, D. E. Pritchard, and W. Ketterle, Phys. Rev. Lett. **89**, 190403 (2002).

[4] N. D. Mermin and T.-L. Ho, Phys. Rev. Lett. **36**, 594 (1976).

[5] T. W. B. Kibble, J. Phys. A **9**, 1387 (1976).

[6] W. H. Zurek, Nature (London) **317**, 505 (1985).

[7] Z. Hadzibabic, P. Krüger, M. Cheneau, B. Battelier, and J. Dalibard, Nature (London) **441**, 1118 (2006).

[8] L. E. Sadler, J. M. Higbie, S. R. Leslie, M. Vengalattore, and D. M. Stamper-Kurn, Nature (London) **443**, 312 (2006).

[9] K. Murata, H. Saito, and M. Ueda, Phys. Rev. A **75**, 013607 (2006).

[10] J. M. Higbie, L. E. Sadler, S. Inouye, A. P. Chikkatur, S. R. Leslie, K. L. Moore, V. Savalli, and D. M. Stamper-Kurn, Phys. Rev. Lett. **95**, 050401 (2005).

[11] T. Isoshima, K. Machida, and T. Ohmi, J. Phys. Soc. Jpn. **70**, 1604 (2001).

[12] H. Saito and M. Ueda, Phys. Rev. A **72**, 023610 (2005).

[13] H. Saito, Y. Kawaguchi, and M. Ueda, Phys. Rev. Lett. **96**, 065302 (2006).

[14] T. Ohmi and K. Machida, J. Phys. Soc. Jpn. **67**, 1822 (1998).

[15] T.-L. Ho, Phys. Rev. Lett. **81**, 742 (1998).

[16] E. G. M. van Kempen, S. J. J. M. F. Kokkelmans, D. J. Hein-zen, and B. J. Verhaar, Phys. Rev. Lett. **88**, 093201 (2002).

[17] J. Stenger, S. Inouye, D. M. Stamper-Kurn, H.-J. Miesner, A. P. Chikkatur, and W. Ketterle, Nature (London) **396**, 345 (1998).

[18] E. A. Kuznetsov and S. K. Turitsyn, Pis'ma Zh. Eksp. Teor. Fiz. **94**, 119 (1988) [Sov. Phys. JETP **67**, 1583 (1988)].

[19] C. T. Law and G. A. Swartzlander, Jr., Opt. Lett. **18**, 586 (1993).

[20] A. V. Mamaev, M. Saffman, and A. A. Zozulya, Phys. Rev. Lett. **76**, 2262 (1996).

[21] Z. Dutton, M. Budde, C. Slowe, and L. Hau, Science **293**, 663 (2001).

[22] A. A. Norrie, R. J. Ballagh, and C. W. Gardiner, Phys. Rev. A **73**, 043617 (2006).

[23] Y. Kawaguchi, H. Saito, and M. Ueda, Phys. Rev. Lett. **96**, 080405 (2006).

[24] L. Santos and T. Pfau, Phys. Rev. Lett. **96**, 190404 (2006).